

Use of Frequency-Randomized SAR Waveforms for the Detection and Mitigation of Small-Motion Effects in Precision RCS Measurement

Keith Morrison

DAPS, Cranfield University
Shrivenham
Swindon SN6 8LA, UK
k.morrison@cranfield.ac.uk

Abstract—The use of SAR and ISAR imaging is an important tool in the laboratory RCS characterization of scattering patterns across signature critical platforms. Despite measures to the contrary, air turbulence and mechanical vibration can produce unwanted complex perturbations of the target during the imaging process. The slow sweep time of many laboratory stepped-frequency CW radars means that a target can undergo significant motion even during a sweep, leading to substantial and time-varying defocusing of range profiles, unsuited to conventional motion-correction schemes. Model code was written to provide simulations of representative complex motions for a string-suspended target. Comparison of images produced using monotonic and randomized waveforms could detail the presence and pattern of very small motion-related changes in RCS. The ability to do this was found to have a complex dependence on the relative lengths of the radar sweep time and the characteristic oscillation period of the motion. When the sweep time and oscillation period are comparable, it may be possible to accurately retrieve the target's entire motion history, from the phase perturbation recoverable from the difference of the monotonic and randomized waveforms in the raw frequency domain. This can then be applied back to the data as a motion correction.

I. INTRODUCTION

Laboratory synthetic aperture radar (SAR) and inverse synthetic aperture radar (ISAR) measurements are used in the characterization and assessment of the RCS scattering patterns of radar signature-critical platforms [1-3]. In the design and assessment of low-observable platforms, exact reproduction of the RCS of each target feature is needed. Because of the cost and logistics of using full sized targets, exact scale models are often used in the assessment exercise [4,5]. With the scale reduction in target size, it is also necessary to scale the radar wavelength accordingly. Thus, to assess the L-band (1GHz) and X-band (10GHz) responses of a $1/10^{\text{th}}$ -scale model, requires use of 10GHz and 100GHz signals, respectively. The use of short wavelengths puts stringent motion stability requirements on the measurement

process in order that coherence is maintained throughout the SAR imaging process. For the frequency range of interest (1-100GHz), even sub-millimeter disturbances can produce significant and unwanted image artifacts.

However, the requirement for high stability and accurate target setting conflicts with the requirement of a very low RCS target support system [6-11]. In order to best mimic a measurement of the target in free space, they are frequently hung by string suspension systems from an overhead gantry at indoor facilities [1,12,13]. Unfortunately, this type of suspension leaves the target vulnerable to mechanical vibration and air turbulence, especially with ISAR imaging which requires rotation of the target relative to a fixed radar. Outdoor measurements, even of full-sized targets, can suffer from wind-induced motion.

The relatively slow sweep time of many laboratory stepped-frequency CW radars [3] means that the target can undergo motion over a significant fraction of a wavelength during the waveform transmit time. Consequently, the resultant defocusing of the range profiles is essentially non-retrievable due to the high dimensionality of the focus parameter space. Well established motion compensation schemes, such as the Phase Gradient Autofocus Technique [14], which rely on the presence of stable and well defined range profiles throughout the imaging process, are not applicable. The simultaneous presence of pendulum-like and twisting torsional-like motion in string suspension systems can make the motion appear complex and chaotic. For string-suspended targets, it is likely that multiple frequencies are present from different resonances of each string support.

This work carries out modeling simulations to understand and quantify the consequences of target motion on SAR imaging schemes obtained with SF-CW waveforms. It looks at using the information obtained by the comparative performance of monotonically-stepped and randomly-hopped waveform, for both the detection and mitigation of target motion and image recovery.

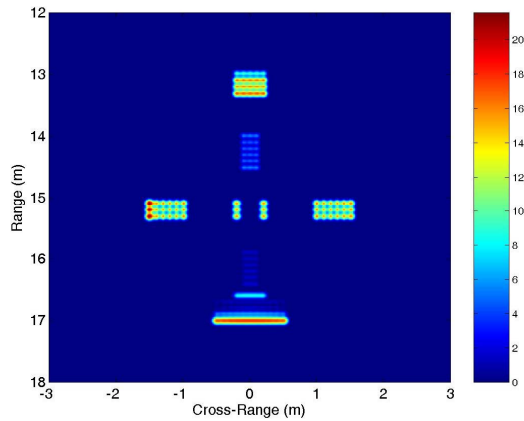


Figure 1. Unperturbed SAR power image of the test body.

II. MODEL

A. Target Motion

A model was written to provide realistic models of the observed motions of string-suspended targets. The model provides for a spatially and temporally varying force pattern at the target for the duration of the imaging process. The target is directly driven by the applied force such that the observed motion of the target can be understood by its reproduction of the force pattern. The model assumes that the target is only subject to motion in the image plane, a criterion largely met for the type of target measurements under consideration where the disturbance is small compared to the target size. The motion information is coded into a simulation of the data acquisition scheme to provide full SAR imagery.

A simulated 4m x 3m test body was constructed from 307-point scatterers, with a variation in scattering amplitude of 30dB. A SAR image of the power variation across the static target is shown in Fig. 1. It consists of a 3.6m (l) x 0.4m (w) fuselage, 0.3m x 1.0m tail section, and approximately half-way down the fuselage and aligned along the cross-range direction, the 0.2m by 3.0m wings. The fuselage is aligned along the boresight direction.

A motion representative of a multi-string suspended target was created. The oscillation is complex and multi-periodic, and is composed of a single ‘normalized’ periodicity of 1.0, plus two time-varying periodicities over the range 0.8 to 0.9. It has a maximum swing of ± 0.8 cm in both range and cross-range. The target behaves as a rigid solid body that traces out the motion locus, but without twisting from its range alignment. There are no obscuration effects, such that each point target is considered to be visible at all times.

B. SAR Imaging Model

The SAR imaging process involves obtaining the discrete radar frequency response, f_l to f_n , of the target at regular

steps across a virtual aperture. In this way the recorded data set is a complex array of the form $D(x, f)$ where x is the scanned distance. It is convenient to consider these data as a superposition of linear arrays, each fixed in frequency but variable in x , in order that the principles of plane-to-plane backward propagation can be exploited for the imaging process [15]. The plane-to-plane technique involves the decomposition of the measured field into its angular spectrum of plane waves.

For all simulations the target was placed at a range centered on 15m, aligned with the centre of the SAR aperture, with a sightline looking down at 10° . Resolution in range was provided by measuring 301 frequencies over a 3GHz bandwidth, B. The frequency step interval of 10MHz provided an unambiguous range of 15m. The simulations are for X-band (10GHz). The target’s radar response was sampled at 501 positions at 1cm intervals to provide a 5m aperture. This provides an equal resolution in range and cross-range of ~ 7 cm. The initial image reconstruction process provides 1cm x 1cm pixels. Spatially averaging was then performed with a sliding boxcar filter over 7 x 7 pixels.

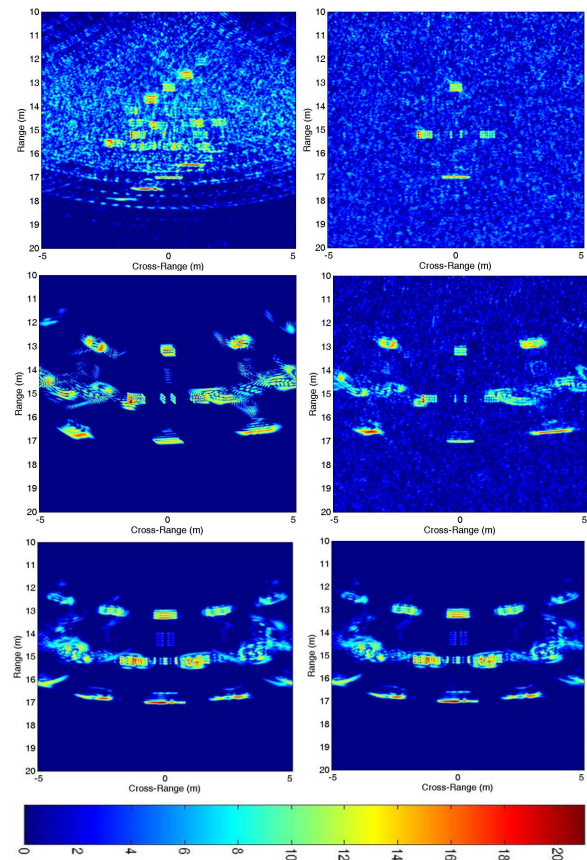


Figure 2. Comparison of images of the test body using monotonic (M, left) and randomized (R, right) waveforms for $\Gamma=0.1$ (bottom), 1.0 (middle), and 10 (top). The images show power over a 21dB dynamic range.

The un-averaged images correspond to power over a 24dB (0-255) dynamic range – however, the averaging process reduces this close to 21dB in the displayed images.

C. Frequency Randomizations

It is usual to collect the frequency data at each aperture position as a monotonically-increasing linear frequency sweep. Thus, n_f frequencies are collected over a bandwidth, at a regular spacing of df , such that $n_f = 1 + B/df$. In the frequency randomization process, exactly the same frequencies are collected, and at the same sampling rate, but the order in which they are collected is randomized from sweep to sweep. The waveform is similar in form to noise radar waveforms [16-19].

III. MODELLING RESULTS

Fig. 2 shows the results of the simulations using monotonic ('M') and randomized ('R') waveforms. It shows that use of a randomized waveform can produce significantly modified imagery. The effect of the randomization on the sidelobe structure was found to be dependent upon the relationship between the 'characteristic' period of oscillation of the target, P_c , and the rate at which the frequency data is collected across a bandwidth. 'Characteristic' is used to define a representative oscillation period for complex or multi-periodic motions. The time taken for the radar to sweep across all frequencies in a bandwidth we denote by T_{sweep} . We refer to the ratio:

$$\Gamma = T_{\text{sweep}} / P_c \quad (1)$$

as the sampling ratio, and is a measure of the fraction of the oscillation each frequency sweep samples, that is, how the radar 'sees' the motion. The monotonic and randomized images are structurally different. The monotonic waveform images show structured sidelobes with distinct features, whereas the randomized waveform sidelobes are broader and less structured. It can be seen that for the slower sweep radar with $\Gamma=10$ (such each frequency sweep is approximately ten times the length of the oscillation period), randomization has produced a significant recovery of the badly motion-degraded result seen with the monotonic waveform. For $\Gamma \leq 1$, randomization has little beneficial effect.

Image recovery is accompanied by an increase in the broadband noise across the entire image. Although the scattering pattern may be largely restored in some instances by randomization with the correct dynamic relationship between the different scattering points on the test body, the absolute power is not recovered. For the simulations using $\Gamma=1$ and 10, the strongest feature within the test body was -11.2 to -13.0dB down on the unperturbed case, respectively. The mean power was similarly reduced by between -12.9dB and -13.3dB. For $\Gamma=0.1$ the reduction was -6.3dB and -6.0dB, identical to the monotonic case.

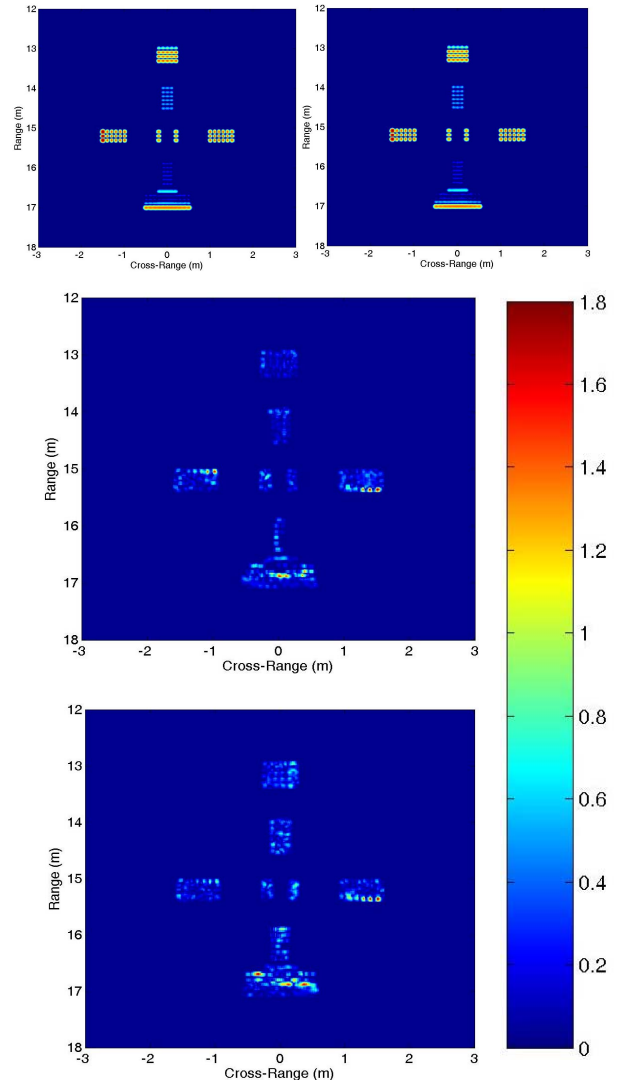


Figure 3. (Top) The monotonic and randomized waveform images over a 21dB scale. The difference images between the monotonic waveform and i) unperturbed (middle), ii) randomized (bottom).

IV. DISCUSSION

A. Very Small Amplitude Motions

The examples of the effects of target motion in Section III were designed to be large and obvious to most clearly illustrate the effects of waveform randomization. Even so, the motion was small $\pm 0.8\text{cm}$, corresponding to movement only $\pm 0.2\%$ of the length of the target, and could easily be overlooked during measurement when close visual examination of the target is difficult. However, the artifacts in the monotonic waveform plots would be suspicious, due to the degradation of the expected image, and because the sidelobes extend spatially to regions where physically there is no target. We ask the question whether the comparison of images using monotonic and randomized waveforms might

be used as a diagnostic to detect much less-obvious motion effects, especially when these lie within the body of the target.

To investigate this idea, simulations for $\Gamma=1.5$ were carried out using the same target motion pattern as previously, but scaled to have only maximum amplitudes of $\pm 0.2\text{cm}$ in range and cross range. Such a motion would be extremely difficult to detect visually. Fig. 3 (top) displays the resulting images for the monotonic and randomized waveforms. Both appear almost identical to the unperturbed case in Fig. 1. A close visual examination shows some very slight changes in the detail of the low-power horizontal barring on the fuselage at the back of the test body between the two waveforms and the unperturbed case. The large images in Fig. 3 show the difference images. The first image shows the absolute power differences between the static case and the monotonic waveform image. Changes of up to 1.47dB are present in the scattering pattern due to target motion. The other image shows power differences between the monotonic and randomized waveform images. Although not an exact one-to-one spatial correlation, both the magnitude and pattern of the discrepant values are similar in the two images, as witnessed by the behavior at the leading edge of the left wing and trailing edge of the right wing, and in the tail section. Thus, for the example given, the differences between the monotonic and randomized waveforms largely replicate the actual differences present due to motion artifacts.

For computational ease both waveforms were considered to have been collected simultaneously with the same imaging geometry. A practical implementation of this might involve the successive transmission of monotonic and randomized waveforms. A more satisfactory case would intertwine the two waveforms, such that they could then be untwined into waveforms more nearly instantaneous with each other.

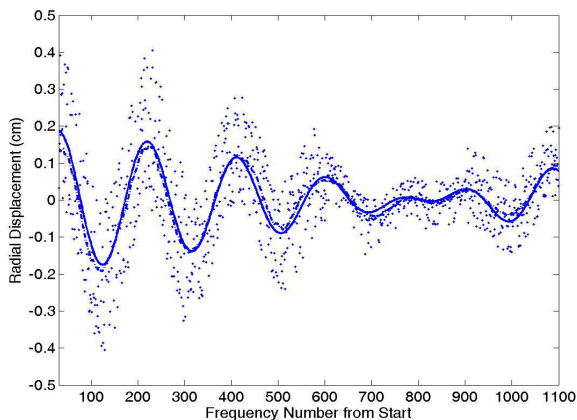


Figure 4. The distribution of ΔR for the first 1,100 data points.

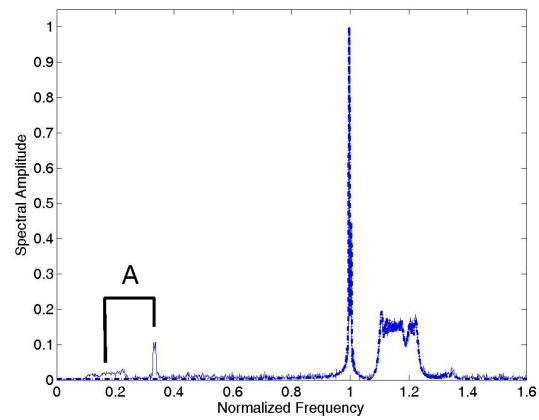


Figure 5 The normalized frequency spectrum derived from FFTs of the ΔR distribution (thin solid line) and the actual radial motion of the test body (thick dash-dotted line). There is excellent agreement between the two traces, apart from the extra features marked 'A'. Both amplitudes are normalized to 1.

B. Recovery of Motion History

Following on from Section IIB, we describe the monotonic and randomized data sets as complex arrays of the form $D_M(x,f)$ and $D_R(x,f)$, respectively. We calculate the phase difference between corresponding array elements as $\text{ang}|D_M(x,f).D_R(x,f)^*|$, where $*$ is the conjugate. If we assume the resulting phase difference, $\Delta\Phi(x,f)$, is due solely to perturbation of the target we can convert this to a radial displacement, ΔR , along the line of sight from the antenna at each data point by:

$$\Delta R(x, f) = \frac{\Delta\Phi(x, f) \lambda_f}{4\pi} \quad (2)$$

where $\lambda_f = c/f$, is the wavelength. Fig. 4 shows the resulting distribution of ΔR for the first 1,100 collected frequency points, corresponding to almost three frequency sweeps (any antenna movement time is ignored). The 4π term in the denominator includes a factor of 2 to convert the measured two-way displacement into a one-way term. There is clearly a periodicity in the distribution of ΔR . The solid line corresponds to the motion history in range seen by the antenna calculated for a point target on boresight at a range of 15m, at the centre of the test body. Although the derived ΔR values represent a coherent summation across all 307 scatterers over the 3m x 4m body, there is very good agreement with the motion history of the point target.

Fig. 5 shows part of the normalized frequency spectrum resulting from an FFT of the ΔR sequence, compared with that from the actual motion history of the test body. There is excellent agreement between the two spectra, apart from the additional features marked 'A' present in the ΔR spectrum. The original motion was constructed a fixed frequency at 1.0, and two variable frequencies in the range 1.1-1.23, which are reproduced correctly. Further investigation indicates that the features marked 'A' are aliases of the true motion frequencies at 1.0 and 1.1-1.23, and their positioning

is dependent upon the sampling of the motion history through the Γ term.

A best fit to the data, shown by the dashed-dotted line in Fig. 4, was found by applying a sliding 60-point average to ΔR , to derive the motion history $\Delta M(x, f)$ of the test body at the time point of each of the 150,801 frequency samples collected in the imaging process. This was then applied as a phase correction directly to the raw data in the monotonic case by $D_M(x, f) \cdot \Delta C(x, f)^*$, where $\Delta C(x, f)^*$ is the phase correction at each frequency point.

Although not attempted here, a more sophisticated motion-correction scheme might seek to apply a differential spatial correction across the target. Application of the motion correction scheme reduced the anomalous scattering discrepancies from 1.47dB to 0.49dB, and significantly modified the detail of the scattering pattern. Although not attempted here, a further examination of any remaining ΔR variations and second motion compensation might improve the result further.

An attempt to use the phase difference between the monotonic waveform and a spot frequency - instead of the randomized waveform - provided no motion information. Likewise, other schemes utilizing the phase differences between monotonic waveforms were also unsuccessful in retrieving the motion history.

REFERENCES

- [1] N. C. Currie, "Radar Reflectivity Measurements: Techniques and Applications". Norwood, MA, Artech House. 1989.
- [2] E. F. Knott, J. F. Shaefter, and M. T. Tuley, "Radar Cross Section," Norwood, MA, Artech House. 1985.
- [3] D. L. Mensa, "High Resolution Radar Cross-Section Imaging". Norwood, MA, Artech House. 1991
- [4] D. Bird. "Target RCS Modelling". In proc. IEEE Radar Conference. p74 – 79. 1994.
- [5] P. Eskelinen, P. Harju, "Low cost arrangements for scale model RCS and pattern measurements". Aerospace and Electronics Conference. Vol. 2, p827-830.
- [6] I. J. LaHaie, "An overview of advanced processing techniques for RCS measurements". IEEE Antennas and Propagation Society International Symposium, Vol. 4, p608 – 611. 2001.
- [7] I. J. LaHaie, E. I. LeBaron, C. J. Roussi, K. Quinlan, "Processing techniques for removal of target support contamination". Antennas and Propagation Society International Symposium, Digest. 2, Vol. 1, p488- 491, 1993.
- [8] J. W. Burns, E. I. Lebaron, G. G. Fliss, "Characterization of target-pylon interactions in RCS measurements". Antennas and Propagation Society International Symposium. Vol. 1, p144 – 147. 1997.
- [9] J. Burns, M. Ricoy, "Investigation of target-support interactions for foam column supports". Antennas and Propagation Society International Symposium. Digest 28, Vol. 3, p1796–1799, 1993.
- [10] J.W. Burns, "Mitigation of target support contamination using an adaptive decomposition technique". Antennas and Propagation Society International Symposium, Vol. 3, p1570-1573,1998.
- [11] J. A. Berrie, G. L. Wilson, "Design of target support columns using EPS foam". IEEE Antennas and Propagation Magazine, Vol. 45, p198-206, 2003.
- [12] J. W. Burns, G. G. Fliss, D. Kletzli, "Modeling and measurement of target-string interactions". Antennas and Propagation Society International Symposium, Digest 1, Vol. 1, p200-203 1996.
- [13] P. J. F. Swart, P. Snoeij, "Point Target Simulation Verification Using Low Level RCS Measurements". Geoscience and Remote Sensing Symposium. Vol. 2, p599–602, 1991.
- [14] P. N. R. Stoye. "ISAR review and progress in algorithms for image focusing". NATO AC/234 Workshop on Radar Imaging and Classification Techniques, 1998.
- [15] J. W. Goodman: "Introduction to Fourier Optics," McGraw Hill, 1978.
- [16] X. Xiaojian and R. M. Narayanan. "FOPEN SAR Using UWB Step-Frequency and Random Noise Waveforms". IEEE Trans. Aerospace and Electronics Systems. Vol. 37, p1287-1300. 2001
- [17] R. M. Narayanan, "Doppler Estimation Using a Coherent Ultrawide-Band Random Noise Radar". IEEE Trans. Antennas and Propagation, Vol. 48, p868-878.
- [18] K. Lukin. "Noise Radar Technology". Telecommunications and Radio Engineering, Vol. 55, 2001
- [19] B.C. Flores, R. F. Jurgens, R. Chiu. "A Random Frequency Hop Code Technique for Improved Range-Doppler Imagery". Antennas and Propagation Society International Symposium, Vol. 3, p2010–2013, 1994.